

Large Hadron Collider Project

LHC Project Report 156

PROTON COLLIMATION IN TEV COLLIDERS

N. Catalan Lasheras, G. Ferioli, J.B. Jeanneret,
R. Jung, D.I. Kaltchev*, T. Trenkler†

Abstract

In high intensity proton colliders with superconducting magnets, quenches induced by beam losses are unavoidable in the absence of a collimation system. We will show that a single stage system cannot suffice at TeV energies. We will discuss a two-stage collimation system at first as an optical system then considering true scattering in collimator jaws. Expected performance at LHC are presented. Then finally, we present the preliminary measurements done at 120 GeV/c in the SPS ring with a simplified three stage collimation system .

*Paper presented at the symposium 'Near Beam Physics'
held at Fermilab, 22 September 1997*

*TRIUMF, 4004 Wesbrook Mall, Vancouver, B.C., Canada V6T2A3,

Member of the Canadian collaboration to the LHC project.

†Formerly CERN-SL Division, now at Siemens-Matsushita OHG, Deutschlandsberg, Austria

Administrative Secretariat
LHC Division
CERN
CH-1211 Geneva 23
Switzerland

Geneva, October 1997

PROTON COLLIMATION IN TEV COLLIDERS

N. Catalan Lasheras, G. Ferioli, J.B. Jeanneret, R. Jung, T. Trenkler*, CERN–SL Division
D. Kaltchev , TRIUMF, Vancouver

1 INTRODUCTION

In high intensity proton colliders with superconducting magnets, quenches induced by beam losses are unavoidable in the absence of a collimation system. We will show that a single stage collimator system cannot suffice at TeV energies. We discuss a two-stage collimation system first as an optical system then considering true scattering in collimator jaws, giving some emphasis to the LHC project. Finally, we present the preliminary measurements done at 120 GeV/c in the SPS ring with a simplified three stage collimation system.

2 PROTON LOSSES AND QUENCH LEVELS

Proton losses can be divided in three basic classes, namely injection, ramping losses and steady losses in collision. In all these cases and in the absence of a collimation system the losses might be concentrated near one location which is the aperture limitation of the ring. The following numerical values are related to the nominal LHC parameters. The effective longitudinal spreading at the loss point is strongly dependent of the local parameters, but can be as low as $\Delta L \approx 10$ m, computed with the average betatronic angle at the effective local vacuum chamber radius.

An injected batch has $N_p = 2.4 \cdot 10^{13}$ protons and is $6 \mu\text{s}$ long. The ratio between actual and tolerable losses is

$$r = \frac{f N_p}{\Delta n_q \Delta L} = 240 \quad (1)$$

with $f = 0.1$ a somewhat arbitrary fraction of the batch lost immediately and $\Delta n_q = 10^9 \text{ pm}^{-1}$ the quench level for fast losses (see below Section 2.1 and Table 2).

At ramping, RF-untrapped protons are not accelerated and migrate slowly towards the vacuum chamber. The flash of losses lasts $\Delta t \approx 0.1\text{s}$, i.e. more than the time needed to make use of the helium trapped in the cable, allowing $\Delta n_q = 2.5 \cdot 10^{10} \text{ pm}^{-1}$ (see below Section 2.1 and Table 2). The full stored intensity is $N_p = 3 \cdot 10^{14}$ protons. With again $f = 0.1$ we obtain using (1) $r = 125$.

In collision, the halo is fed by elastic scattering in $7 + 7$ TeV collisions, at a rate of $\dot{n}_{el} \approx 10^9 \text{ ps}^{-1}$ for two experiments with $\mathcal{L} = 10^{34} \text{ cm}^{-2} \text{ s}^{-1}$ and $\sigma_{el} = 40$ mbarn. The scattered protons are emitted at an angle close to the beam divergence at the crossing point [1] and slowly enlarge the transverse beam tail. Losses associated to transverse diffusion related to machine imperfections are estimated from SPS collider experience.

* Formerly CERN–SL Division, now at Siemens-Matsushita OHG, Deutschlandsberg, Austria

Table 1: Maximum density of energy deposited in the coil magnet by a proton impacting the vacuum chamber at the betatronic angle (see text).

| p [TeV/c] | ε_{max} [J cm ⁻³] | L_{eff} [m] | ε_{dist} [Jm cm ⁻³] |
|-----------|---|---------------|---|
| .45 | $1.4 \cdot 10^{-11}$ | 1.0 | $1.4 \cdot 10^{-11}$ |
| 7 | $9.2 \cdot 10^{-10}$ | 0.7 | $6.5 \cdot 10^{-10}$ |

With a lifetime of $\tau_{beam} \approx 50$ hours the losses would be $\dot{n}_{beam} = N_p / \tau_{beam} \approx 2 \cdot 10^9 \text{ ps}^{-1}$, for a total $\dot{N}_{loss} = \dot{n}_{beam} + \dot{n}_{el} \approx 3 \cdot 10^9 \text{ ps}^{-1}$. The steady quench level will be $\dot{n}_q \approx 8 \cdot 10^6 \text{ pm}^{-1} \text{ s}^{-1}$ (see below Section 2.2 and Table 3). In this case $r = \dot{N}_{loss} / (\dot{n}_q \Delta L) = 30$, without taking into account large fluctuations of the losses associated to short term instabilities of the beam halo.

In all three cases, the factor r is much larger than the allowed value $r = 1$. The sole good way to lower r is to use collimators which both absorb protons or dilute in phase and amplitude those one that are scattered back into the aperture of the ring.

2.1 Transient quench levels

This section summarises the content of the report [2]. The transient quench level of a magnet is quantified basically by the amount of energy per unit volume ΔQ which is needed to raise the temperature of the coil above its critical value T_q . To compute the number of protons lost locally which induce a quench, the average shower (hadronic and electromagnetic) developed by a proton impacting the vacuum chamber near the coil of the magnet was simulated with the CASIM code [3]. This allows to compute the maximum density of the energy release ε_{max} by the shower in the coil. In practice, apart from a few pathological cases, the proton losses are spread over distances longer than the effective length of the showers $L_{eff} \sim 1$ m. Therefore, instead of ε_{max} , the quantity $\varepsilon_{dist} = \varepsilon_{max} L_{eff}$ is used. Numerical values are given in Table 1.

The number of protons Δn_q which must be lost locally to induce a quench is

$$\Delta n_q = \frac{\Delta Q}{\varepsilon_{dist}} \quad (2)$$

where Δn_q has the units protons m^{-1} . For a given T_q , the heat reserve is the integral of the specific heat between the bath of helium $T_o \approx 1.9\text{K}$ and T_q with $T_q \approx 9\text{K}$ at injection beam energy and $T_q \approx 2.8\text{K}$ at top beam energy.

The heat reserve $\Delta Q(T_q)$ depends also on the duration of the transient loss. The cable of the coil is made of wires

Table 2: Heat reserve and allowed transient losses of protons at injection momentum (upper part) and top momentum (lower part) in LHC, see text. First two lines, metallic contribution only. Third line with trapped helium included. The uncertainty on these values is about $\pm 50\%$.

| Δt [ms] | ΔQ [J] | ε_{dist} [Jm/cm ⁻³] | Δn_q [pm ⁻¹] |
|-----------------|--------------------|---|----------------------------------|
| < 3 | $4 \cdot 10^{-2}$ | $3.8 \cdot 10^{-11}$ | 10^9 |
| 6 | $4 \cdot 10^{-2}$ | $1.4 \cdot 10^{-11}$ | $3 \cdot 10^9$ |
| > 50 | $35 \cdot 10^{-2}$ | $1.4 \cdot 10^{-11}$ | $2.5 \cdot 10^{10}$ |
| Δt [ms] | ΔQ [J] | ε_{dist} [Jm/cm ⁻³] | Δn_q [pm ⁻¹] |
| < 1 | $8 \cdot 10^{-4}$ | $1.3 \cdot 10^{-9}$ | $6 \cdot 10^5$ |
| 3 | $8 \cdot 10^{-4}$ | $6.5 \cdot 10^{-10}$ | $1.2 \cdot 10^6$ |
| > 10 | $3 \cdot 10^{-2}$ | $6.5 \cdot 10^{-10}$ | $4.6 \cdot 10^7$ |

closely packed in an insulator, through which the helium flows too slowly to contribute in the case of transient losses (see next section). On the other hand, the heat reserve of the helium trapped between the wires contributes but the heat transfer is limited by the film of bubbles which develops at the interface of the two media above a critical value. The critical volumetric transfer of power is estimated to $\phi_V = 8 \text{ Wcm}^{-3}$ at injection and $\phi_V = 4 \text{ Wcm}^{-3}$ at 7 TeV. The critical time scale to allow the use of the trapped helium is thus $\Delta t = \Delta Q(T_q)/\phi_V$. The contribution of the helium to $\Delta Q(T_q)$ is integrated numerically using experimental data [4].

At shorter time scale, the sole metallic part of the cable contributes to $\Delta Q(T_q)$. In spite of some modifications related to the superconducting state of the NbTi, the specific heat of the wires is dominated by the cubic dependence on T of the Debye theory. The contribution of the metal to $\Delta Q(T_q)$ is therefore small at 7 TeV when compared to the one of the helium, even if the last one occupies only five per cent of the volume of the cable.

At a further smaller time scale $\delta t \sim 2\text{ms}$, below the temperature decay time across the section of the cable, ε_{dist} must be multiplied by a factor 2-3, to take into account the radial variation of the energy deposition inside the cable $\varepsilon_{dist}(r)$. Above that critical value, the average radial value can be used.

Δn_q as computed with (2) for the three different time scales discussed is given in Table 2. Linear interpolation can be used between the characteristic time scales, keeping in mind that all values are certainly not more precise than a factor two.

2.2 Steady quench levels

The steady power which can be evacuated by the coils while staying below the critical temperature is related to the electrical insulation of the cables. The heat is evacuated off the cables by the exchange of helium through this insulator. The allowed flux of energy per unit volume of cables given in Table 3 are the result of a compromise between the electrical resistivity and the porosity of the insulator. These

Table 3: Allowed steady losses of protons (see text). The uncertainty on these values is about $\pm 50\%$.

| p [TeV/c] | W_q [W] | ε_{dist} [Jm/cm ⁻³] | \dot{n}_q [p(ms) ⁻¹] |
|-----------|-------------------|---|------------------------------------|
| .45 | 10^{-2} | $1.4 \cdot 10^{-11}$ | $7 \cdot 10^8$ |
| 7 | $5 \cdot 10^{-3}$ | $6.5 \cdot 10^{-10}$ | $8 \cdot 10^6$ |

values are measured on sample coils. The allowed steady rate of protons is given by $\dot{n}_q = W_q/\varepsilon_{dist}$.

The comparison of the allowed transient losses $\Delta Q = 8 \cdot 10^{-4}$ J at the time scale $\Delta t = 3 \cdot 10^{-3}$ s (top energy, table 2) with the amount of energy removed by steady conduction during the same time $\delta Q_{cond} = W_q \Delta t = 1.5 \cdot 10^{-5}$ J, indicates that close to their upper limit transient losses rely only on local heat reserve.

3 A SINGLE COLLIMATOR AND TRANSVERSE DIFFUSION OF THE HALO

To be efficient, a primary collimator must be placed inside the short term dynamic aperture (short term meaning here < 1000 turns). In the LHC it will be at a normalised transverse depth of $n_1 = x/\sigma_x \sim 6$. In this range of amplitudes, the transverse drift speed v_d of the halo cannot be predicted either precisely or reliably. At the CERN antiproton-proton collider, in collision somewhat below the beam-beam limit, an experiment indicated $v_d \approx 3 \sigma/s$ at $n_1 = 6$ [5]. LHC tracking data without ripple at injection energy indicate $v_d < 0.05 \sigma/s$ [6]. For given v_d , a distribution of impact parameter, parametrised by a range Δb is obtained by a simple multiturn tracking. Some values are given in Table 5. The computed Δb must be compared to the critical impact parameter b_c , beyond which an impacting proton is more likely to be absorbed instead of being scattered out of the jaw by multiple coulomb scattering or nuclear elastic scattering (this last process being ignored in the rest of this section). The computation of b_c is made in section 3.2. By comparing Δb to b_c in Table 5, we can conclude that in LHC, at least at injection we will be in a regime of strong outscattering.

3.1 Side escape by multiple coulomb scattering

Multiple coulomb scattering is described by the Moliere theory, which is a formalism of diffusion applied to a large number of small successive transverse kicks applied to a charged particle passing through matter [7]. The number of scatterers per millimeter is very high. Both the angular distribution, with the polar angle θ , $dN/d\theta_{mcs}(s)$ and the spatial transverse one $dN/d\Delta_{mcs}(s)$ of the protons around the original axis of flight are gaussian up to ~ 3 standard deviations. The dependence on a given monoatomic material is contained mostly in the radiation length L_R (see Table 4). The standard deviations of $dN/d\theta_{mcs}(s)$ and $dN/d\Delta_{mcs}(s)$ are (with units m and TeV/c)

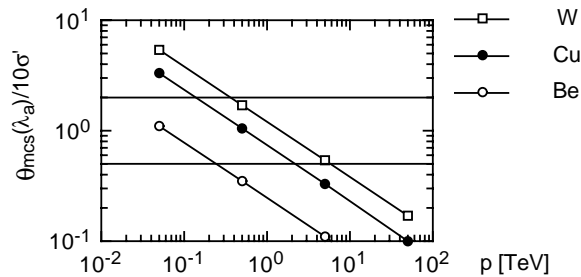


Figure 1: The m.c.s angle after one absorption length, normalised to an effective machine aperture of 10 r.m.s beam units for different materials. The two lines delimit the momentum range in which the outscattering density is high in the aperture of the ring.

Table 5: An estimator of the impact parameter range Δb of the proton in LHC computed with $v_d = 1 \sigma/s$, at the normalised transverse distance from the beam axis $n_1 = 6$, compared to the critical impact parameter b_c below which outscattering by the collimator edge is important.

| p [TeV/c] | Δb [μm] | b_c [μm] |
|-------------|------------------------------|-------------------------|
| .45 | 4 | 12 |
| 7 | 1 | 0.7 |

$$\theta_{mcs}^o(s) = \frac{13.6 \cdot 10^{-6}}{p} \left(\frac{s}{L_R}\right)^{1/2}$$

$$\text{and } \Delta_{mcs}^o(s) = \frac{7.8 \cdot 10^{-6}}{p} \left(\frac{s^3}{L_R}\right)^{1/2}. \quad (3)$$

Disregarding edge escape, the proton flux is attenuated exponentially along the collimator by nuclear absorption, with the absorption length $\lambda_{abs}(Z)$ (see Table 4). The angular distribution of the protons escaping a collimator can therefore be estimated using (3) with $s = \lambda_{abs}(Z)$. This quantity, normalised to an effective machine aperture of $10\sigma'$, where σ' is the r.m.s beam divergence at the collimator location, is plotted in Figure 1 for different materials. Two cases are favourable for collimation. At low momentum ($p < 100 \text{ GeV}$), and using a heavy target, the scattered protons are spread much beyond the aperture. Most of them are lost nearby the collimator and the rest is strongly diluted in the aperture area. At high energy ($p > 10 \text{ TeV}$), by using a light target, the scattered protons stay well inside the aperture. They will do many turns and finally be absorbed by the collimator which is their sole obstacle at small amplitude. In the intermediate momentum range (the case of LHC), a high intensity cannot be cleaned by a single collimator, if the beam loss rate is high in the sense of Section 2.

3.2 Critical impact parameter

The critical impact parameter b_c is computed by using (3) with again $s = \lambda_{abs}(Z)$. The quantity $\lambda_{red}(Z) =$

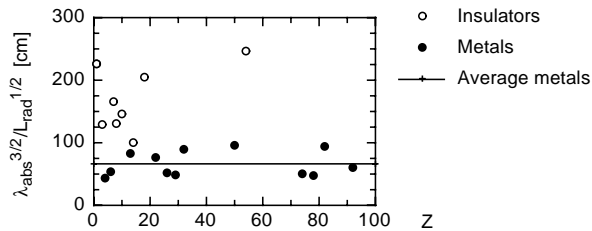


Figure 2: The reduced length λ_{red} as a function of the atomic number Z . For metals (black dots), λ_{red} is nearly constant with an mean value $\lambda_{red} = 0.66 \text{ m}$ and a relative variance $\sigma(\lambda_{red})/\lambda_{red} = 0.3$.

$(\lambda_{abs}^3/L_R)^{1/2}$ is given in Figure 2 for several materials. Interestingly, the metals of interest for collimation (good heat conductivity and good vacuum properties) all have a similar λ_{red} , with no visible dependence on Z . Thus, the critical impact parameter is approximately metal-independent and equal to (with units μm and TeV).

$$b_c = 5.2/p. \quad (4)$$

3.3 Secondary collimator material

The wide angular range of protons scattered off the primary collimator implies a somewhat uniform distribution of impacts on the secondary collimators. Provided they are long enough ($\sim 5\lambda_{abs}$), tertiary particles will be mostly issued from a surface layer of thickness b_c . The Z -independence of b_c therefore allows to choose freely the material of the secondary collimators. Other parameters will be considered (physical length and radiation length, thermal conductivity, resistance to shock waves for exemple).

3.4 Secondary collimators needed

At Tev energies, the outscattering rate off a primary collimator is close to unity. The use of a two-stage collimation system is therefore mandatory.

4 OPTICS AND COLLIMATION

The material discussed here is fully developed in [8],[9] and [10], to which the reader can refer for more details and full demonstrations. In this section we do not consider true scattering in collimators, which is introduced in Section 6. We only do optics and geometry in the four dimensional phase space. We consider the primary collimators as pure isotropic scatterers and secondary collimators as black absorbers. Our criterion to define an optimal two-stage collimation system is to minimise the surface occupied by the secondary halo in the plane of the normalised amplitude $A_X - A_Y$, or the largest distance to the origin of this same surface as it is delimited by the secondary collimators.

Table 4: The nuclear absorption and the radiation lengths in metric units for some Z -values. Cross-sections are valid in the few hundred GeV range. σ_{dd} at 450 GeV/c. λ_{abs} and L_R in [cm]. All cross-sections in [mbarn]. b_{pN} in [$\text{GeV}^{-2}c^2$].

| Element | Z | A | λ_{abs} | L_R | σ_{abs} | $\sigma_{pN,el}$ | n_{pp} | $\sigma_{pn,el}$ | σ_d | b_{pN} |
|---------|-----|------|-----------------|-------|----------------|------------------|----------|------------------|------------|----------|
| H | 1 | 1 | 720 | 865 | 33 | - | - | 7 | 3.4 | 12.0 |
| Be | 4 | 9 | 40 | 35 | 200 | 70 | 3.2 | 22.4 | 11 | 75 |
| Al | 13 | 27 | 39 | 8.9 | 420 | 210 | 4.7 | 32.7 | 16 | 120 |
| Cu | 29 | 63.5 | 15 | 1.4 | 780 | 450 | 6.2 | 43.4 | 21 | 220 |
| W | 74 | 207 | 9.6 | 0.35 | 1650 | 1120 | 9.2 | 64.4 | 31 | 450 |

4.1 Numerical example

To illustrate numerically some results and to help comparing different systems with each other, we will use some identical basic parameters in further sections. The jaws of the primary collimators will always be retracted by $n_1 = 6$ normalised transverse r.m.s. beam radius and the jaws of the secondary collimators always by $n_2 = 7$. All other quantities will be deduced from these two numbers. These numbers are presently a kind of canonical set used for LHC collimation studies. They can of course be changed to any other value for another application.

4.2 Normalised coordinates

The phase coordinates (z, z') of the two transverse directions are normalised at each point along the ring with

$$\mathbf{Z} = \begin{pmatrix} Z \\ Z' \end{pmatrix} = \frac{1}{\sigma_z} \begin{pmatrix} 1 & 0 \\ \alpha_z & \beta_z \end{pmatrix} \begin{pmatrix} z \\ z' \end{pmatrix} \quad (5)$$

z standing here for either the x or y direction, s being the longitudinal coordinate, $\alpha(s)$ and $\beta(s)$ the Twiss functions and $\sigma = (\epsilon\beta(s))^{1/2}$ the transverse r.m.s beam size. The transfer matrix M_{12} transporting a particle from s_1 to s_2 in the normalised coordinates (Z, Z') is then simply the rotation

$$M(\mu) = \begin{pmatrix} \cos \mu & \sin \mu \\ -\sin \mu & \cos \mu \end{pmatrix} \quad (6)$$

with μ being the betatronic phase advance between s_1 and s_2 . The betatronic motion is thus reduced to a harmonic motion, where the betatronic phase advance plays the role of the time, or of the longitudinal coordinate s . In the normalised phase space, the invariant amplitude of a particle in one transverse direction (or 2D-phase space) is $A = (Z^2 + Z'^2)^{1/2}$. The 4D-amplitude is $A = (A_x^2 + A_y^2)^{1/2}$.

4.3 One dimensional betatronic collimation

The proton which drifts slowly outwards touches the collimator when being very close to its maximum spatial extension $\mathbf{Z}_o = (n_1, 0)$ (Figure 3). By scattering in the collimator it gets an angular kick $Z' = K_z$, distributing uniformly

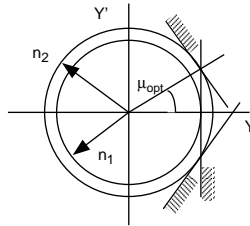


Figure 3: One dimensional betatronic collimation. A particle is scattered close to its maximum transverse position $Z = n_1$. If it is not absorbed, it is scattered along the vertical line $Z = n_1$. If a secondary collimator is at the depth n_2 , the shortest cut along this line is made with a secondary collimator at the phase advance μ_{opt} .

the protons along the line $\mathbf{Z}_1 = (n_1, K_z)$. The sole free parameter to choose the location of a secondary collimator is the phase advance μ between the primary collimator and the secondary collimator. The minimisation of the secondary halo amplitude is done by cutting the line $Z = n_1$ with a secondary collimator at the phase advance [8]

$$\cos \mu_{opt} = \pm \frac{n_1}{n_2}. \quad (7)$$

The maximum secondary amplitude escaping the two-stage collimation system is the absolute possible minimum $A_{cut}^{min} = n_2$ which is equal to the secondary collimator aperture. This is obtained by transporting \mathbf{Z}_1 at μ_{opt} , or $\mathbf{Z}_2 = M(\mu_{opt})\mathbf{Z}_1$. Then, using (7) it follows $Z_2 = n_1^2/n_2 + (1 - n_1^2/n_2^2)^{1/2}K_z$. Cutting at $Z_2 = n_2$ finally gives $K_{cut} = K_z = (n_2^2 - n_1^2)^{1/2}$ and $A = (Z_1^2 + K_{cut}^2)^{1/2} = n_2$. The two signs in (7) corresponds to cutting each of the two half lines $Z = n_1, Z' > 0$ and $Z' < 0$.

4.4 Two dimensional betatronic collimation in $X - Z$ symmetric optics

The particular optics which has the property $\mu_x(s) = \mu_y(s)$ (or equivalently $\beta_x(s) = \beta_y(s)$) was studied because a soft symmetric low- β insertion, which has this property, was envisaged for a time for the cleaning system of LHC [11]. Later, it appeared that this particular case is the sole one which we have been able to treat analytically. We use it here to show that a two dimensional collimation system

is not a simple extension of the one dimensional case discussed above.

The closest extension of the one dimensional system in two dimensions is the use of circular collimators (circular in normalised coordinates, approximated for example by eight jaws in a real case), with a radial aperture n_1 for the primary collimator and n_2 for the secondary collimators. To simplify the present discussion, we consider only the impact point on the primary collimator at $(X, Y) = (n_1, 0)$. The treatment of the other azimuth is done in [8]. The non trivial difference with a one dimensional system appears at the impact point in the primary collimator where scattering populates every azimuthal direction in the $X' - Y'$ plane.

Let us write the coordinates of the proton before scattering

$$\mathbf{A}_o = (X, X', Y, Y') = (\mathbf{X}, \mathbf{Y}) = (n_1, 0, 0, 0) \quad (8)$$

We limit our discussion to two extreme cases, which we call parallel and orthogonal scattering. Parallel means scattering in the plane of the original betatronic oscillation, i.e. $(X', Y') = (k_x, 0)$ in our case of azimuth. Orthogonal scattering is when $(X', Y') = (0, k_y)$.

Parallel scattering leaves intact the Y-amplitude, i.e. $A_y = 0$ before and after scattering. The problem is therefore reduced to the one dimensional case and is solved by installing two circular collimators at $\cos \mu_{opt} = \pm \frac{n_1}{n_2}$.

The coordinates of the proton after orthogonal scattering are

$$\mathbf{A}_1 = (\mathbf{X}_1, \mathbf{Y}_1) = (n_1, 0, 0, k_y) \text{ with } k_y \in [-\infty, \infty]. \quad (9)$$

In the absence of coupling, there is no way to cut on the X-amplitude $A_X = n_1$ which is smaller than the secondary collimator aperture n_2 . To cut efficiently on the Z-amplitude, we must place an additional secondary collimator where the angle is entirely converted to amplitude, i.e. at phase advance $\mu = \pi/2$ from the primary collimator. \mathbf{A}_1 transforms to

$$\mathbf{A}_2 = (M(\pi/2)\mathbf{X}_1, M(\pi/2)\mathbf{Y}_1) = (0, -n_1, k_y, 0) \quad (10)$$

The secondary collimator cuts on Y at $k_z \leq n_2$. The largest vector leaving that collimator is then

$$\mathbf{A}_2 = (n_1, 0, n_2, 0) \text{ with } A_2 = (n_1^2 + n_2^2)^{1/2}. \quad (11)$$

A_2 is the largest combined amplitude passing the secondary collimators and occurs in the case of orthogonal scattering. The intermediate cases between parallel and orthogonal scattering are cut in amplitude at values in the range $A \in [n_2, A_2]$ [8]. The limits are identical at other $X - Y$ azimuths. With our numerical set, the secondary halo extends up to $A_2 = 9.2$.

The important result is that, at least in the kind of optics used in this section, with optimal secondary collimator locations, the cut in amplitude is done at a value somewhat larger than the secondary collimator aperture. We will see

that this result remains true in any kind of optics, if the cleaning section is of reasonably finite length.

Other optics

FODO optics of different phase advance per cell were explored, by fitting the circular collimator locations with numerical methods [8]. The result, expressed by the largest secondary amplitudes was always less performant than the symmetric low-beta section discussed here above.

Rectangular collimators

If the number of collimators is an issue or conversely, if the geometrical aperture of the ring is large enough, rectangular collimators (X and Z jaws only) can be used. The degradation of the performance in amplitude cut relative to circular collimators is $\sim 20\%$ [8].

5 LOCATING COLLIMATORS IN ARBITRARY OPTICS. THE LHC CLEANING INSERTION.

The general case of finding the best solution of primary and secondary collimator locations in an arbitrary optics requires a numerical approach. The DJ code [9],[10] allows to locate both in longitudinal position and $X - Z$ azimuth an arbitrarily large number of jaws (here and below, jaw stands for a pair of transversely opposite jaws). It is found more efficient at the same hardware cost to abandon the use of circular collimators, anyway approximated by eight flat jaws, and to let the location and the azimuth of every jaw free in the fit. The number of free parameters is therefore $N_{par} = 2N + 3 = 27$ for the equivalent of three circular collimators ($3 \cdot 8$) and three primary jaws, the last ones being kept horizontal, vertical and skewed at 45° . The function to be minimised can be the radius A_{max} of the smallest circle surrounding the geometrical edge of the secondary halo. A_{max} is not a smooth function and classical minimum finding methods often fail to find a good solution. The simulated annealing method [12] is used instead. This algorithm always find several good solutions, allowing to choose one which does not create hardware conflicts.

Several FODO like optics were tried for LHC, with different phase modulation $\mu_z - \mu_x$. The better result $A_{max} = 8.4$ is obtained for the largest achievable $(\mu_z - \mu_x)$ in an insertion which has a total phase advance $\mu_x \approx \mu_z \approx 2\pi$ (see Figure 4). Our interpretation of the result is that a large phase modulation allows to catch more of the 'orthogonally' scattered protons (Section 4.4). On this point, see also [13]. The absolute value of A_{max} is quite good and anyway better than the optimum reached with the symmetric insertion of Section 4.4.

6 SCATTERING AND COLLIMATION EFFICIENCY

The approach used in section 4 and 5 which allows to fit collimator locations in a given optic and to choose between different optics do not allow to compute the efficiency of

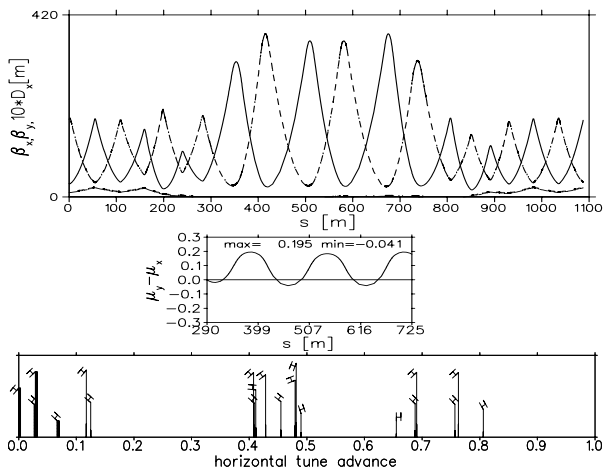


Figure 4: IR7 lattice and tune-split functions for LHC version 5.0, with the IR7 quadrupoles tuned for high positive tune split, giving $A_{max} = 8.45\sigma$. The range of tune advance (in 2π units) corresponds to the range $s \in [290, 725]$.

a system. True scattering in matter in both primary and secondary collimators is needed. The complexity of a two-stage collimation system implies to use numerical methods. Even the simple case of scattering near the edge of a block of matter cannot be treated analytically. In this section, we discuss only elastic interactions. Inelastic interactions are discussed in Section 8.

Elastic scattering must be coupled to multiturn tracking in the ring. Elastic scattering near the edge of a media was treated exhaustively for the first time, to our knowledge, by Andy van Ginneken [14]. Our own code K2 [15] was inspired by his ELSIM program. The K2 code is made of a scattering module, does tracking between collimators in a beam line section described with the MAD format, does an amplitude analysis and closes a turn if the particle was not absorbed. To ensure an approximately realistic distribution of impacts on the primary collimator, the proton is circulated inside the primary aperture using linear motion superimposed with a variable transverse drift speed until it touches a collimator. We gave some emphasis to fast algorithms, to allow for the large statistics needed to compute high collimation efficiencies.

Halo drift

Halo protons become unstable through transient resonant states or experience chaotic motion. The detailed mechanism of losses might depend strongly on operational conditions of the machine. An average case is used for collimator studies. We use a smooth variable transverse drift speed v_d . We verified that the calculated collimation efficiency do not vary strongly over a quit large range v_d with a two-stage collimation system, while it is obviously not the case with a single stage system.

Tracking in collimator

While in Section 3 we considered multiple coulomb scattering to show the importance of edge scattering, nuclear scattering of protons on both nuclei and the nucleons inside the nuclei is of similar importance. This is shown by computing a weighted ratio of average scattering angles (mcs and elastic scattering on individual nucleons, and using the data of Table 4) in a Cu target as

$$r = \frac{\theta_{pp,elastic}}{\theta_{mcs}(1\lambda_{abs})} \frac{\sigma_{pp}^{Cu}}{\sigma_{inel}^{Cu}} = 0.5 \quad (12)$$

We only briefly describe how we parametrise nuclear elastic processes. In this report, the soft momentum dependence of some parameters is neither shown or discussed. This will be the object of a more exhaustive document [16]. Nuclear elastic processes can to a very good degree of precision be described by an optical model. The incident wave diffracts on a grey object of density decreasing transversely with a Gaussian law. The angular distribution of the distribution is the Fourier transform of the density of the target, i.e. it is also Gaussian. Its standard deviation $\sigma(\theta)$ is related to the effective radius R_{eff} of the proton-target compound. The Lorentz invariant $t = (p\theta)^2$ is usually used and the angular distribution is written

$$\frac{d\sigma}{dt} = \sigma_{el} b e^{-bt}. \quad (13)$$

The parameter b is related to R_{eff} with

$$R_{eff} \approx 0.4b^{1/2} \quad [\text{fermi}, (\text{Gev}/c^2)^2] \quad (14)$$

and σ_{el} is the elastic cross-section.

A proton can scatter both on nuclei (noted N) and on nucleons (noted n) inside the nucleus. Proton and neutrons are treated identically. In addition to elastic scattering, the incident proton do diffractive dissociation on nucleons.

Proton-nucleon elastic scattering

Proton-nucleon (pn) elastic scattering has been much studied [17],[18]. For our purpose, the approximate differential cross-section (13) is adequately precise, accounting for most of the cross-section. From data at 20 GeV/c [19] and at 175 GeV [20], we deduce that pp elastic scattering is not visibly modified when occurring inside a nucleus. In particular, no trace of double elastic scattering is observed. The equivalent number of free scatterers, as measured by [19] can be modelled with a simple geometrical model, considering that only the nucleons located near the equator in a plane perpendicular to the incoming proton contributes to the cross-section. The dependence of the cross-section on the atomic mass A is fixed by adjusting the thickness of the contributing layer. We get a number of individual scatterers per nucleus

$$n_{pn} = 1.56A^{1/3}. \quad (15)$$

The pn elastic cross-section is then $\sigma_{pn}(A) = n_{pn}\sigma_{pp,el}$. In the TeV range (LAB frame), $\sigma_{pp,el} \approx 8.5 \text{ mb}$ and $b \approx 13 \text{ GeV}^{-2}$.

Single diffractive dissociation

The single diffractive dissociation process is close to elastic scattering but the excitation of one of the nucleons, to a mass M larger than the nucleon mass m_n is done at the expense of a relative momentum loss $\delta_p = -\Delta p/p$ of the nucleon staying intact. The case of the incident proton staying intact is of interest here. The other case is treated like an inelastic interaction (see Section 8). The variables δ_p and M are related by (at low-order approximation)

$$\delta_p \approx \frac{M^2}{s} \approx \frac{M^2}{2m_n p} \quad (16)$$

with s the centre of mass energy squared and m_n the nucleon mass. The double differential cross-section can be approximated by [17]

$$\frac{d^2 \sigma}{d\delta_p dt} = \frac{a_d b_d}{\delta_p} e^{-b_d t} \quad (17)$$

We use $b_d = (7/12)b_{pp,el}$, while $a_d \approx 0.7mb$ [17]. The mass range is $M \in [M_o, (0.15s)^{1/2}]$. We use the approximation $M_o \approx m_n \approx 1 \text{ GeV}/c^2$. With (16), we compute a momentum range $\delta_p \in [M_o/(2p), 0.15]$. The integral cross-section is $\sigma_{d,pn} = n_{pn} a_d \ln(0.15s) = n_{pn} a_d \ln(0.3p)$.

Proton-nucleus scattering

Total proton-nucleus (pN) cross-section are reported in [7]. They are almost constant in the few hundred GeV/c momentum range. Elastic pN (or coherent) cross-sections are found at the same source, while the differential elastic cross-section are found in [20] at 175 GeV/c. Some of these values are given in Table 4. Non measured values (W) are interpolated with $A^{1/3}$ or $A^{2/3}$ laws, which fit well the data [20], [16]. A slight momentum dependence is given to the data in Table 4. It is related to the pn scattering, which has an impact on the total cross-section. We consider that the coherent cross-section cannot rise significantly at high energy for the nucleus to be already a black absorber below 1 TeV/c. The formula (13) is adequate to describe the data, except for very heavy nuclei where secondary and tertiary diffraction peaks are visible in data [20]. This is explained by the blackness of the high- A nuclei up to their edge. But even for lead ($A = 82$), the relative integral of the second peak is only 5% of the elastic scattering cross-section, while the heaviest target to be considered in practice would be tungsten ($A = 74$). Numerical values can be found in Table 4.

Algorithm for multiple coulomb scattering

In the neighbourhood of the edge of a collimator jaw, multiple coulomb scattering, which is a quasi continuous scattering process needs a special treatment. The obvious method of doing small steps is precise but time consuming. The complete m.c.s. formalism shows that using the correlation factor $\rho_{\theta\Delta} = \sqrt{3}/2$ between the angle and the transverse offset (both following Gaussian distributions of

variances (3)), an arbitrarily large step can be made without biasing the result. The actual step is computed as the distance at which the transverse offset $\Delta = 4\Delta_{mcs}^o$ coincides with the edge of the jaw. This procedure, even if it requires to solve a 3rd-order equation at each step is very fast. When the impact parameter is large enough, the jaw is traversed in one step, if other interactions do not occur [16].

The large angle tail of Coulomb, or Rutherford, scattering is treated as a discrete interaction. The cross-section is the integral of the differential cross-section above $\theta \geq 4\theta_{mcs}^o$ [16].

Tracking from collimator to collimator

The protons are transported by standard linear transfer matrices [21]. Drift spaces, bending magnets and quadrupoles are considered. To allow the use of linear transfer matrix elements in the relative momentum deviation δ_p , a cut-off is made at $\delta_p < 1\%$. Those protons scattered beyond that momentum are treated like inelastic collisions (Section 8).

Check of ring aperture and collimator efficiency

Doing an aperture control all along the ring is very time consuming. Step tracking and a detailed and coherent model of misalignments (magnetic and mechanic) and closed orbit defaults would be needed. While this kind of analysis is under work, up to now we checked the combined amplitude of the proton at the end of the cleaning section. Above a specified amplitude (in general close to the effective geometrical aperture of the ring), the proton is considered to have touched the vacuum chamber and the tracking is stopped. Below this cut-off amplitude, at each turn the amplitude is recorded in a so-called survival plot (see Section 7 and Figure 5 for an example), which gives the relative number of proton surviving a given amplitude F_s . Then, off-line, the betatronic phase-space plots are analysed. A lower limit of the longitudinal dilution of the losses is given by the approximative formula

$$F_d \approx 1/2\pi\beta \quad (18)$$

and by using for β the smallest of β_x and β_z near the aperture limitation. This formula is valid if the dilution in phase is almost homogeneous (checked with the phase-space plot). Then the efficiency of the system, for a given aperture limitation, is

$$\eta_{ring} = F_s(A_{ring}) F_d \quad (19)$$

Closing a machine turn

A proton surviving the aperture control is transported in one step to the beginning of the cleaning section, with a linear transfer matrix. The sole non-linear effect introduced in K2 is some tune smearing of adjustable range. The actual tune is drawn randomly following a truncated Gaussian distribution at each turn.

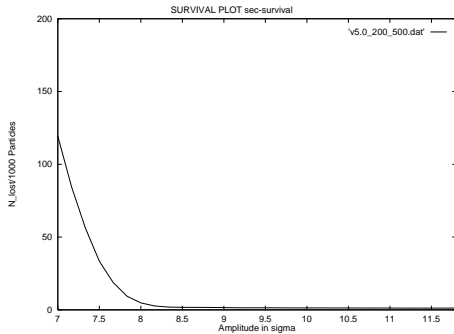


Figure 5: The survival plot in LHC at injection with the cleaning insertion described above, see text. In abscissa, the radial betatronic amplitude A_r . In ordinate, the function $F_s(A_r)$, normalised to 1000 events touching a primary collimator. See text.

Table 6: Expected efficiency of the betatronic cleaning insertion.

| p [TeV/c] | F_s - | F_d [m^{-1}] | η [m^{-1}] | η_{DS} [m^{-1}] | m |
|--------------|-------------------|------------------------------|-------------------------------|------------------------------------|---------------|
| .45 | $2 \cdot 10^{-3}$ | $5 \cdot 10^{-3}$ | 10^{-5} | 10^{-5} | ≈ 40 |
| 7 | $4 \cdot 10^{-4}$ | $5 \cdot 10^{-3}$ | $2 \cdot 10^{-6}$ | 10^{-5} | ≈ 330 |

7 USING K2 FOR LHC COLLIMATION

A preliminary calculation of the efficiency of the LHC cleaning insertion (see Section 5) was made with the K2 code. The primary collimators were made of 200 mm long Aluminium jaws while the secondary collimator jaw are made of Copper and 500 mm long. The survival plot at injection energy (Figure 5) indicate that the effective edge of the secondary halo is close to the amplitude $A_{sec} = 8$, a value slightly better than the geometrical edge computed by DJ (Section 5). The relative flux of protons F_s above $A_{sec} = 8.4$ is given in Table 6. The longitudinal dilution F_d of these protons along the ring is computed with (18) using $\beta = \beta_{min,arc} \approx 30$ m.

Efficiency margin in the ring

The margin factor m in Table 6 is either

$$m = \frac{\Delta n_q}{f N_p \eta} \quad \text{or} \quad m = \frac{\dot{n}_q}{\dot{N}_{loss} \eta} \quad (20)$$

Comparing (20) to (1) indicates that an effective length of dilution of the halo after collimation can be defined by $L_{eff} = \eta^{-1}$.

Another efficiency factor, η_{DS} , is related to losses in the dispersion suppressor which is adjacent to the collimation system. Protons issued from diffraction dissociation and lower momentum particles (mostly neutrals ones) are swept out by the bending magnets and are lost locally. The effect is minimised by the presence of the warm bending magnets of the so-called dog-leg structure of the collimation insertion [23] but cannot be avoided completely. It

limits locally the efficiency at top energy.

The margin factor is computed with the largest of η and η_{DS} .

An earlier simulation (LHC V4.2) was compared to a simulation with the STRUCT code [24]. Both calculations agree to better than a factor three for η .

The margins look comfortably large but high values are needed. It must be remembered that beam losses are partly of erratic nature. A spicky time structure can strongly lower the margin temporarily. The ring aperture is also dependent of the operation. Lowering the aperture of the ring by one normalised unit near A_{sec} drops the margin by nearly one order of magnitude.

7.1 Halo rates upstream of experiments

Residual halo rates near experiments are estimated by integrating the fraction of the protons which escape the cleaning area and are captured by the aperture limitation upstream or at an experiment. We consider first the case of a so-called Roman pot, i.e. an abrupt change of the pipe aperture made of two half-planes, separated by $\pm n_{pot}$ r.m.s beam sizes. Protons of amplitude $A = A_{ring} \approx 30$ must be inside a phase window $\Delta\mu = \pm \cos^{-1}(n_{pot}/A_{ring})$ to touch the pot. Protons of amplitude $A < n_{pot}$ never touch the pot. With an amplitude distribution $dN/dA \sim const$ above $A_{sec} \approx 10$ (see Section 7), it follows that out of the fraction F_s of the protons surviving the collimation system, the subfraction $F_{pot} = 0.5\Delta\mu/2\pi \approx 0.33$ touches the pot, with $n_{pot} \approx 15$. The overall rate with nominal LHC parameters shall therefore be (see Section 2)

$$\dot{n}_{pot} = F_{pot} F_s \dot{N}_{loss} = 3 \cdot 10^5 \text{ ps}^{-1}. \quad (21)$$

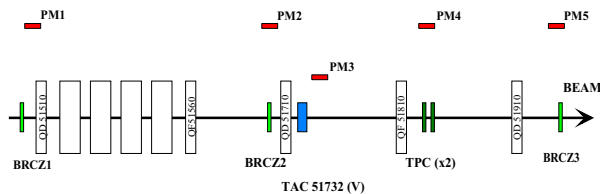
Near experiments installed in a low-beta insertions, both $\beta_x(s)$ and $\beta_z(s)$ grow to very large values. We can use $F_{low-beta} \approx 1$ and therefore (21) becomes $\dot{n}_{low-beta} \approx 10^6 \text{ ps}^{-1}$. These rates are comparable to beam-gas losses at the same locations. Their impact in terms of muon backgrounds have been carefully computed [22].

8 INELASTIC INTERACTIONS IN DISPERSION SUPPRESSORS NEAR COLLISION POINTS

Downstream of collision points, most of secondary particles issued from inelastic interactions are lost in the adjacent triplet of quadrupoles and in the beam separation magnets [25], but the forward protons of diffractive dissociation will be lost where the dispersion grows, i.e. after entering the dispersion suppressor. Their impact can be estimated in a simple way. It is shown in [26] that in a section with a vacuum pipe of fixed radius, the rate of diffractive losses per unit length along the pipe is $\dot{n} = \mathcal{L} a_d D'/D$, with $\mathcal{L} = 10^{34} \text{ cm}^{-2} \text{ s}^{-1}$, $a_d = 0.7 \text{ mb}$, $D(s)$ the local dispersion and $D' = dD/ds$. In the high luminosity insertions of LHC, $(D'/D)_{max} \approx 0.07$ and therefore $\dot{n}_{max} = 5 \cdot 10^5 \text{ m}^{-1} \text{ s}^{-1}$. With a steady quench level at $\dot{n}_{max} = 8 \cdot 10^6 \text{ m}^{-1} \text{ s}^{-1}$, the margin factor is $m \approx 16$ and is reduced to $m \approx 6$ with the ultimate luminosity

LHC Collimation studies. Coast at 120 GeV

Experimental layout on LSS5



Goal: Estimate the rate of protons lost on each collimator as a function of their relative apertures. Compare with the simulations.

Figure 6: The experimental layout of the SPS collimation experiment at 120 GeV/c.

$\mathcal{L} = 2.5 \cdot 10^{34} \text{cm}^{-2} \text{s}^{-1}$. There is little chance for the luminosity to grow erratically above its design value. The margin factor is therefore adequate. A small degradation of the margin must be expected if magnet misalignments and closed orbit effects are taken into account.

9 EXPERIMENTAL WORK

In order to validate the K2 code an experiment was made in April 1997 at the SPS accelerator. A 120 GeV proton beam was made to coast. Its intensity was $N_p \approx 10^{12} \text{p}$. The beam was debunched and made to slowly diffuse transversely by injecting some wideband noise in the kHz range through a damper. The noise level was adjusted to set the loss rate to $\dot{n}_{loss} \approx 5 \cdot 10^8 \text{ps}^{-1}$. Three horizontal collimators, called BRCZ1, 2 and 3 in Figure 6, were installed in a weakly radioactive straight section. They are made of two opposite 250 mm long Aluminium jaws. The phase advance between the collimators was $\mu_{1-2} = 90^\circ$ and $\mu_{1-3} = 200^\circ$. The length and the material were chosen to get collision rates of the same order of magnitude in the three collimators. A system aiming at highest efficiency (thicker secondary jaws) would have made the rate at the tertiary collimator too low for reasonable conditions of measurements. A vertical collimator, made of two $4 \lambda_{abs}$ jaws (stainless steel), was installed at $\mu_{1-v} = 90^\circ$ to keep under control the large amplitude scattered protons.

9.1 Detection of interactions

The most immediate observable which is proportional to the collision rate in a collimator is the rate of inelastic interactions. The detection of elastic collisions would require to install telescopes in the vacuum chamber and would be affected by a large background because of the thick target. Inelastic interactions, on the other hand develop a shower of which low energy particles escape at large angle.

A detailed simulation with the code GEANT [27] allowed to compute the energy deposition in scintillation counters (surface 35cm^2 , thickness 1 cm) placed near the collimators. To avoid the saturation of the photomultipli-

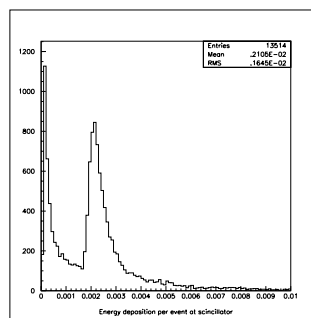


Figure 7: The analog spectrum in the scintillator as simulated with GEANT.

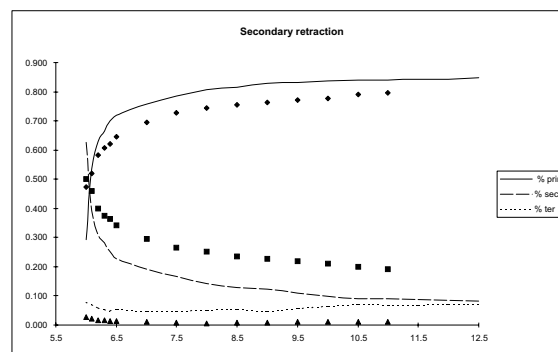


Figure 8: The raw relative rates measured at the collimators. Diamonds and upper curve: PRIM, squares and medium curve: SEC, triangles and lower curve: TER. Points are raw measurements (for some corrections see text). The curves are the result of multi-turn tracking and scattering in jaws made with the K2 code. The wavy structures on the curves are of statistical nature. The data analysis is preliminary.

ers, the counters were placed 90 cm above the beam line. The rate right above the collimator is small and grows with the distance when moving downstream. A broad maximum is reached at a distance of 65 cm downstream of the centre of the collimator. Installed at that location the counters are almost insensitive to a position error and the simulated yield is $Y_{pm} \approx 3 \cdot 10^{-3}$, with a maximum rate in operation $\dot{n}_{pm} = Y_{pm} \dot{n}_{loss} \approx 3 \cdot 10^5 \text{counts s}^{-1}$.

One sample of the analog spectrum to be recorded at the counters is shown in Figure 7. Minimum ionising particles traversing the scintillator populate the second peak. Very low energy electrons and photons converted to photoelectrons populate the first peak. To best control the calibration a threshold for counting was fixed near the lower edge of the second peak. The counters were calibrated in a high energy tertiary muon beam of the SPS fixed target beams.

9.2 The measurements and their simulation.

The principle of the measurements is to set all the collimators at their respective transverse position n_i , measured in normalised units. We use the notation n_1 for the primary

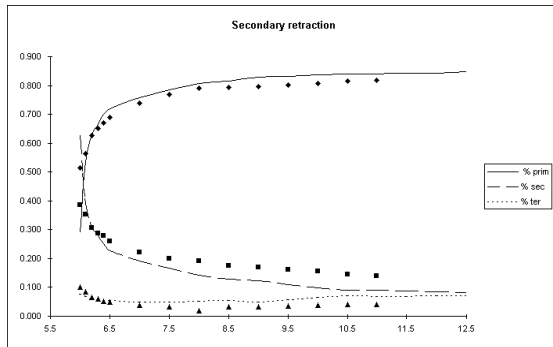


Figure 9: The adjusted relative rates measured at the collimators. The data are adjusted to the simulation (curves) by leaving free two parameters, see text. The data analysis is preliminary.

collimator (PRIM), n_2 for the secondary collimator (SEC), n_3 for the tertiary collimator (TER) and n_v for the vertical collimator (VERT). The nominal positions are $n_1 = 6$, $n_2 = 7$, $n_3 = 10$ and $n_v = 8$. At the horizontal collimators, $\Delta n_i = 1$ is equivalent to 0.8 mm. We recorded the rates of the four counters, varying n_2 (SEC retraction) by steps $\delta n = 0.5$ in the range $n \in [6, 11]$.

The origin of the n_i scales is found by removing all the jaws except one. Then, its opposite jaw is pushed towards the beam by small steps, until a spike of losses indicates that the mobile jaw is more inside the aperture than the fixed one. The losses are monitored and displayed continuously with a time integration of ≈ 10 ms to allow this measurement. The procedure is repeated for all the collimators. The closed orbit (CO) at the collimator is the average of the two positions when the spike occurs. We estimate the CO error to $\sigma(n) \approx 0.5$.

The proportionality between the normalised and the real position is given by the computed beta functions, with an error likely to be smaller than 5%. The raw data are presented in Figure 8. We ran K2 for every set of n_i positions. Many small effects on the data are taken into account. A non exhaustive list includes the variation of the GEANT yields Y_{pm} with the distance between two opposite jaws or with the impact parameter distribution changing with different relative retractions. The absolute loss rate during the data acquisition time of one set of positions (≈ 10 s) cannot be measured with adequate precision. It would rely on the beam current transformer, which shall have a resolution of at least $\dot{I}/I \approx 10^{-4}$ to be useful. The data are therefore presented as fractions of unity. No relative factors between collimators were introduced, and only the data relative to the three BRCZ (which are identical) are compared. The agreement in both shape and amplitude of the data at the primary and the secondary collimators is quite good. The tertiary rate on the other hand is quite below the simulation.

To evaluate the importance of the discrepancy, we let a cross-calibration coefficient to vary between the three rates, to fit better to the K2 simulation. In Figure 9, the SEC data are multiplied by $f_{SEC} \approx 0.7$ and the TER data by

$f_{TER} \approx 3$. More work is needed to determine if the discrepancy observed with the tertiary data is of experimental nature or related to the K2 algorithms (while we have a preference for the first hypothesis).

If the present results are not fully satisfactory from a physics point of view, on the other hand they are quite good in view of the design of a collimator system. The measured rates at the tertiary collimator being smaller than the predicted ones, the last ones shall be used to compute the expected efficiency of the collimator system

10 MOMENTUM COLLIMATION

Momentum collimation is not discussed here, but its need at LHC is established (see section 2). The formalism to design an insertion exists [8], and a case study is going on, using an updated version of the DJ code [10].

11 REFERENCES

- [1] L.Burnod and J.B. Jeanneret, CERN SL/91-39(EA), LHC Note167,1991.
- [2] J.B.Jeanneret et al,CERN LHC project report 44,1996.
- [3] A.van Ginneken,CASIM,Fermilab TN 309,1978.
- [4] R.D.McCarty,NBS Tech.Notes 1029 and 1972.
- [5] L.Burnod et al.,CERN/SL/90-01(EA),LHC Note 117,1990.
- [6] N.Catalan Lasheras and J.B.Jeanneret, CERN LHC project Note 101,1997.
- [7] Review of Particle Properties,Phys.Rev. D45,1992.
- [8] T.Trenkler and J.B.Jeanneret, Particle Accelerators, 50,287(1995) and the bibliography therein.
- [9] D.I.Kaltchev et al.,EPAC96,Barcelona,June 1996 and CERN LHC Proj.Rep.37,1997..
- [10] D.I. Kaltchev et al.,PAC97,Vancouver,June 1997 and CERN LHC Proj.Rep.134,1997.
- [11] Design of the Large Hadron Collider,CERN 91-03, 1991
- [12] A.Corona et al.,ACM Trans. on Math.Soft.13,p262,1987.
- [13] T. Risselada,CERN SL/Note 95-67(AP),1995.
- [14] A.van Ginneken,Phys.Rev.D37,p.3292,1988.
- [15] T.Trenkler,J.B.Jeanneret,CERN SL/Note94-105(AP),1994.
- [16] to appear in N.Catalan Lasheras,Ph.D.,1998.
- [17] K.Goulios,Physics Report 101,No3,p.169,1983.
- [18] G. Matthiae,Rep.Prog.Phys,57,p743,1994.
- [19] C.Belletini et al.,Nucl.Phys.79,p.609,1966.
- [20] A.Schiz et al.,Phys.Rev.D21,p.3010,1980.
- [21] K.L.Brown et al.,CERN 80-04,1980.
- [22] Workshop on LHC backgrounds,K.Potter ed.,CERN,1996.
- [23] The Large Hadron Collider,CERN/AC/95-05(LHC),1995.
- [24] A.I.Drozhdin and N.V.Mokhov,PAC97,Vancouver,1997.
- [25] N. N.Mokhov and J.B.Strait,PAC97,Vancouver,1997.
- [26] J.B.Jeanneret,CERN/SL/92-44(EA),LHC Note 211,1992.
- [27] GEANT,Application Software Group,CERN,March 1995.